Efficient Computational Model for Inductive Plasma Flows

David Vanden Abeele* and Gérard Degrez†
von Kármán Institute for Fluid Dynamics, B-1640 St. Genesius-Rode, Belgium

A new approach to the numerical modeling of high-pressure inductive plasmas is presented. The governing magnetohydrodynamic equations are discretized in a second-order accurate finite volume manner. A pressure-stabilized flowfield solver is introduced as an alternative to the staggered-mesh solvers used in traditional algorithms. It is argued that the widely used integral boundary formulation for the electric field is computationally expensive and cannot be incorporated into an efficient iterative solution procedure. A far-field formulation of the electric field is adopted instead, such that state-of-the-art iterative methods can be applied to speed up the calculation. The discretized equations are solved through a damped Picard method and an approximate and a full Newton method. Efficient linear algebra methods are used to solve the linear systems arising from the iterative methods. An appropriate linearization of the (strongly positive) joule heating source term is found to be important for the convergence at the linear level. The new model is tested on a 3-species argon and an 11-species air inductive plasma computation. The proposed damped Picard iterative method is found to be very robust during the initial iterations, but does not converge well thereafter. The approximate Newton method converges substantially better. Finally, the full Newton method yields rapid quadratic convergence rates at the expense of an increase in storage. Taking into account both speed of convergence and memory use, the approximate Newton method is considered to be optimal.

Nomenclature

CFL	= damping parameter similar to the Courant number
$D\{J\}$	= block diagonal of the Jacobian/Picard matrix J
E	= total electric-field amplitude (complex quantity), $V \cdot m^{-1}$; global vector containing electric-field variables
$\boldsymbol{E}$	= total electric field (radio frequency), $V \cdot m^{-1}$
E_P	= electric-field amplitude generated by plasma (complex quantity), $V \cdot m^{-1}$
E_V	= electric-field amplitude generated by inductor in absence of plasma (complex quantity), $V \cdot m^{-1}$
F^r	= radial component of Lorentz force per unit volume, $N \cdot m^{-3}$
F^z	= axial component of Lorentz force per unit volume, $N \cdot m^{-3}$
f	= torch operating frequency, Hz
f_m	= discrete mass flux in axial direction, $kg \cdot m^{-2} \cdot s^{-1}$
h	= internal enthalpy per unit mass, $J \cdot kg^{-1}$
I_C	= current through outer inductor, A
J_E	= electric-field Jacobian matrix
J_P	= Picard matrix
J_Q	= total Jacobian matrix
J_U	= flowfield Jacobian matrix
n_e	= Number density of electrons, m^{-3}
P_{joule}	= joule heating source term, $W \cdot m^{-3}$
P_{rad}	= radiative loss term, $W \cdot m^{-3}$
p	= static pressure, $N \cdot m^{-2}$
Q	= total solution vector (flowfield plus electric field)
$q_{z,r}$	= conductive heat fluxes, $W \cdot m^{-2}$
R	= inner radius of quartz tube, m
$Re_{\Delta z}$	= Reynolds number based on cell length in z direction
R_E	= electric-field residual
R_Q	= total residual
R_U	= flowfield residual
r	= radial distance from torch axis, m
T	= temperature, K
U	= flowfield vector
$\boldsymbol{u} = (u, v, w)$	= velocity (axial, radial, and azimuthal components), $m \cdot s^{-1}$
z	= axial distance from torch inlet, m
β	= estimated maximal velocity in the flowfield, $m \cdot s^{-1}$
$\delta(\boldsymbol{r} - \boldsymbol{r}_C)$	= Dirac δ distribution; equals zero everywhere except near the infinitely thin inductor rings, where it is singular
Λ	= effective thermal conductivity, $W \cdot m^{-1} \cdot K^{-1}$
μ	= dynamic viscosity, $kg \cdot m^{-1} \cdot s^{-1}$
μ_0	= vacuum magnetic permeability, $kg \cdot m \cdot C^{-2}$
ρ	= density, $kg \cdot m^{-3}$
σ	= electrical conductivity, $\Omega^{-1} \cdot m^{-1}$
τ	= tensor of viscous stresses, $N \cdot m^{-2}$

Subscripts

A	= indicates an ambient quantity (e.g., outlet pressure)
E	= indicates an average value on a cell edge
E, U, Q	= electric field/flowfield/flowfield plus electric field
i	= number of considered torch inlet ($i = 1$ corresponds to central injection)
L, R	= indicates reconstructed values to the left and the right, respectively, of a given cell edge
l	= loops over all cells appearing in the computational stencil
R, I	= indicates the real and imaginary parts, respectively, of the electric-field amplitude E
wall	= indicates properties of quartz tube wall
z, r, θ	= in the axial, radial, or azimuthal directions, respectively

Superscripts

$\tilde{F}$	= indicates that numerical stabilization has been added to the discrete convective flux F
$\tilde{J}$	= indicates an approximation to the Jacobian matrix J
n	= indicates a step in the iterative procedure
T	= transpose of indicated array

*Ph.D. Candidate, Department of Aeronautics and Aerospace, 72 Steenweg-op-Waterloo; vdabeele@vki.ac.be. Student Member AIAA.
†Professor, Department of Aeronautics and Aerospace, 72 Steenweg-op-Waterloo. Senior Member AIAA.

Introduction

IN a high-pressure inductively coupled plasma (ICP) torch, a gas is heated in an electrodeless manner to a plasma with peak temperatures of $\sim 10,000$ K. The gas, usually at atmospheric pressure, is injected into a quartz tube surrounded by a copper inductor. A radio-frequency electrical current runs through the inductor and induces a secondary current through the gas inside the quartz tube, which heats up by means of ohmic dissipation. Figure 1 shows a small atmospheric argon ICP torch in operation. Inductive plasmas are used in a wide variety of industrial and scientific applications.[1] In the aerospace industry, air ICPs at relatively high pressures of 0.01–0.1 atm are used to test thermal protection systems for atmospheric (re)entry vehicles.[2,3] High-pressure ICPs are close to thermochemical equilibrium, in contrast with low-pressure inductive discharges, in which nonequilibrium processes play a dominant role.[4]

In the three decades since the first two-dimensional model of Miller and Ayen[5] appeared, considerable progress has been made in the modeling of high-pressure ICPs.[6] Milestones in this field are the models of Boulos,[7] Mostaghimi et al.,[8] and McKelliget.[9] The elegant formulation of the time-averaged axisymmetric magnetohydrodynamic (MHD) equations developed by these authors underlies the majority of contemporary high-pressure ICP models. The modeling of low-pressure ICPs has been progressing toward similar pseudosteady axisymmetric MHD formulations (see Ref. 10), even though the physics involved differs considerably.

Although quite accurate and physically relevant, the current high-pressure ICP models still require a lengthy iterative process for converging. The discretized equations are solved in a sequential manner, which considerably slows down convergence. Underrelaxation needs to be applied to ensure the stability and the convergence of the numerical procedure. A large number of semi-implicit iterations is needed to converge; at each iteration, thermodynamic and transport property models need to be reevaluated. When complex mixtures such as 11-species air are simulated, the evaluation of these models becomes a major cost. To keep computational times reasonable, it is then desirable that the model converge in a minimal number of iterations.

This contribution aims at improving the computational speed and accuracy of the existing high-pressure ICP models, rather than introducing new physics. It is argued that, provided the electric field is properly discretized, powerful iterative methods may be applied to speed up numerical calculations. A robust Picard method may be used to obtain a first, approximate solution. Thereafter, a Newton method may be used to converge rapidly to machine accuracy. Most high-pressure ICP models rely on classical staggered-mesh incompressible flow solvers.[11] As an alternative, an easily programmable pressure-stabilization approach[12] has been used in the present study.

Governing Equations

Axisymmetric Local Thermodynamic Equilibrium Model of the Torch

The torch is modeled by a fully axisymmetric configuration (Fig. 2). To this end, the outer inductor is represented by a series of parallel current-carrying rings. 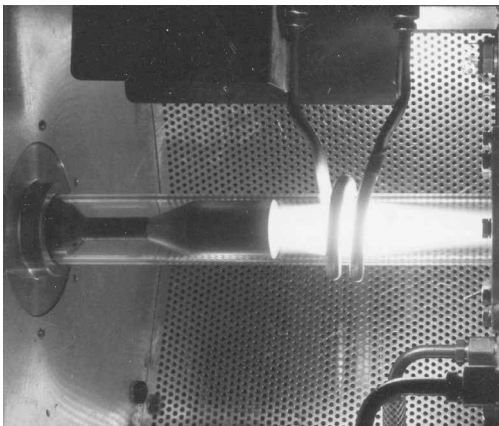For simplicity, the current rings are assumed to be infinitely thin. The plasma is considered to be in a state of local thermodynamic equilibrium (LTE). This approximation holds if the operating pressure is not too low[13] and the operating frequency is not too high.[14] As Reynolds numbers are rather low (~ 500), the flowfield is taken to be laminar. These assumptions enable us to considerably simplify the governing equations[15] and to focus on the numerical aspects of the model.

Magnetohydrodynamic Induction Equation

All electromagnetic phenomena may be expressed in terms of the azimuthal electric field, which consists of a single Fourier mode:

$$\boldsymbol{E} = E \exp(i2\pi f t)\boldsymbol{e}_\theta$$

where f represents the operating frequency of the torch. To take into account phase differences within the plasma, the electric-field amplitude E stands for a complex variable. The electric-field amplitude can be shown to satisfy the following fully resistive MHD induction equation, both inside the torch and on a far-field domain that covers the space around the torch[16]:

$$\frac{\partial^2 E}{\partial z^2} + \frac{1}{r}\frac{\partial}{\partial r}\left(r\frac{\partial E}{\partial r}\right) - \frac{1}{r^2}E - i2\pi\mu_0\sigma f E$$

$$= -i\mu_0 2\pi f \delta(\boldsymbol{r}-\boldsymbol{r}_C)I_C \qquad (1)$$

where the Dirac δ distribution on the right-hand side takes care of the singular current density in the (infinitely thin) inductor rings. For the radio-frequency currents used in high-pressure ICPs, it is reasonable to assume that a single coil current with amplitude I_C oscillates at phase angle zero through each coil ring.[10]

Local Thermodynamic Equilibrium Flowfield Equations

The radio-frequency electromagnetic field generates small oscillating perturbations on all flowfield quantities. When the flow equations are averaged in time, a quasi-steady flowfield formulation similar to the Navier–Stokes equations is obtained. In the momentum equation, a time-averaged Lorentz force appears; in the energy equation a time-averaged joule heating source term appears.

The continuity, momentum, and energy equation are cast under an axisymmetric conservative form:

$$\frac{\partial r F^c}{\partial z} + \frac{\partial r G^c}{\partial r} = \frac{\partial r F^d}{\partial z} + \frac{\partial r G^d}{\partial r} + S \qquad (2)$$

The convective fluxes F^c and G^c are given by

$$F^c = [\rho u, \rho u^2 + p, \rho uv, \rho uw, \rho uh]^T$$

$$G^c = [\rho v, \rho vu, \rho v^2 + p, \rho vw, \rho vh]^T \qquad (3)$$

The contribution of kinetic energy to the enthalpy may be neglected at operating pressures greater than 0.01 atm, for which inductive
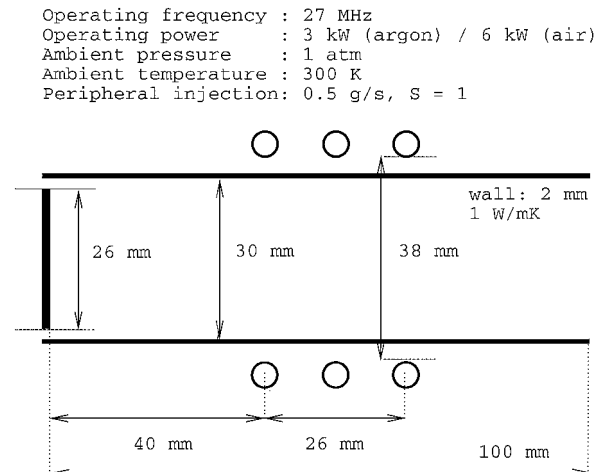

Fig. 1 Small ICP torch in operation (von Kármán Institute minitorch, argon, 0.5 g/s, 45-deg swirl, 1 atm, 3 kW, 27 MHz).

```
Operating frequency : 27 MHz
Operating power     : 3 kW (argon) / 6 kW (air)
Ambient pressure    : 1 atm
Ambient temperature : 300 K
Peripheral injection: 0.5 g/s, S = 1
```


Fig. 2 von Kármán Institute minitorch geometry and operating conditions used for the numerical simulations.

plasma flows are characterized by low Mach numbers (<0.3). The diffusive fluxes F^d and G^d are given by

$$F^d = [0, \tau_{zz}, \tau_{zr}, \tau_{z\theta}, q_z]^T, \qquad G^d = [0, \tau_{rz}, \tau_{rr}, \tau_{r\theta}, q_r]^T \quad (4)$$

The shear stresses τ_{ij} may be further expressed as

$$\tau_{zz} = 2\mu\frac{\partial u}{\partial z} - \frac{2}{3}\mu\left(\frac{\partial u}{\partial z} + \frac{\partial v}{\partial r} + \frac{v}{r}\right), \qquad \tau_{zr} = \tau_{rz} = \mu\left(\frac{\partial u}{\partial r} + \frac{\partial v}{\partial z}\right)$$

$$\tau_{rr} = 2\mu\frac{\partial v}{\partial r} - \frac{2}{3}\mu\left(\frac{\partial u}{\partial z} + \frac{\partial v}{\partial r} + \frac{v}{r}\right)$$

$$\tau_{z\theta} = \mu\frac{\partial w}{\partial z}, \qquad \tau_{r\theta} = \mu\frac{\partial w}{\partial r} \quad (5)$$

The conductive heat fluxes are given by

$$q_z = \Lambda\frac{\partial T}{\partial z}, \qquad q_r = \Lambda\frac{\partial T}{\partial r} \quad (6)$$

The contribution of viscous dissipation is much smaller than the effect of thermal conduction and has therefore been neglected in the energy equation. The source term S is given by

$$S = [0, rF_z, p + \rho w^2 - \tau_r + rF_r, -\rho vw - \tau_\theta, rP_{\text{joule}} - rP_{\text{rad}}]^T \quad (7)$$

The remaining shear stresses τ_r and τ_θ may be expressed as

$$\tau_r = -\frac{2}{3}\mu\left(\frac{\partial u}{\partial z} + \frac{\partial v}{\partial r} - 2\frac{v}{r}\right), \qquad \tau_\theta = \mu\frac{w}{r} + w\frac{\partial\mu}{\partial r} \quad (8)$$

With the real and the complex parts of the electric-field amplitude indicated by E_R and E_I, respectively, the time-averaged Lorentz forces F_z and F_r are written as

$$F_z = \frac{\sigma}{4\pi f}\left(\frac{E_R}{r}\frac{\partial rE_I}{\partial z} - \frac{E_I}{r}\frac{\partial rE_R}{\partial z}\right)$$

$$F_r = \frac{\sigma}{4\pi f}\left(\frac{E_R}{r}\frac{\partial rE_I}{\partial r} - \frac{E_I}{r}\frac{\partial rE_R}{\partial r}\right) \quad (9)$$

Finally, the time-averaged joule heating source term is given by

$$P_{\text{joule}} = (\sigma/2)(E_R^2 + E_I^2) \quad (10)$$

Most ICP models assume, for mathematical convenience, that radiation is optically thin.[7] Radiative losses may then be modeled through a straightforward loss term P_{rad} in the energy equation.

Boundary Conditions
Electric Field
The electric field should be zero on the axis and at infinity:

$$E(z, 0) = 0, \qquad E(z, \infty) = 0, \qquad E(\pm\infty, r) = 0 \quad (11)$$

Flowfield
At the torch axis, symmetry of the solution is imposed:

$$\frac{\partial\rho u}{\partial r} = 0, \qquad \frac{\partial\rho w}{\partial r} = 0, \qquad \frac{\partial T}{\partial r} = 0$$

$$\frac{\partial p}{\partial r} = 0, \qquad \rho v = 0 \quad (12)$$

The torch outlet is taken as corresponding to a discharge in an ambient space:

$$p = p_A, \qquad \frac{\partial\rho\boldsymbol{u}}{\partial z} = 0, \qquad \frac{\partial T}{\partial z} = 0 \quad (13)$$

On the quartz tube inner surface, no-slip boundary conditions are imposed and the temperature is obtained when heat flux continuity is imposed at the plasma/quartz interface:

$$\frac{\partial p}{\partial r} = 0, \qquad \rho\boldsymbol{u} = 0, \qquad \Lambda\frac{\partial T}{\partial r} = \Lambda_{\text{wall}}\frac{T_A - T}{d_{\text{wall}}} \quad (14)$$

The flow is injected in an annular manner through various inlets, situated at radial positions of $R_{i-1} < r < R_i$. For torches without central injection, an adiabatic no-slip condition is imposed at $r < R_0$. The axial inlet momentum Q_i is to be calculated from a given total mass injection rate. The model allows for an azimuthal inlet momentum component, which is taken to be a swirl number S_i times the axial inlet momentum. This translates into the following inlet boundary condition:

$$r < R_0 : \rho\boldsymbol{u} = 0, \qquad \frac{\partial p}{\partial z} = 0, \qquad \frac{\partial T}{\partial z} = 0$$

$$R_{i-1} < r < R_i : \rho u = Q_i, \qquad \rho v = 0, \qquad \rho w = S_i Q_i$$

$$\frac{\partial p}{\partial z} = 0, \qquad T = T_A \quad (15)$$

Physical Modeling
LTE plasma thermodynamic properties are computed from statistical thermodynamics, and plasma transport properties are computed with the method of Chapman and Enskog (see Ref. 17). Optically thin radiative losses may be included in curve-fitted form, based on experimental or theoretical results.[18] It is common practice to disregard optically thick radiative losses.[7]

We have not found any justification for the assumption of an optically thin plasma. Dresvin et al.[19] state that both optically thin and thick radiation need to be taken into account; however, an adequate modeling of optically thick radiation appears to be very difficult. Fortunately, radiative losses decrease strongly with pressure[18] ($P_{\text{rad}} \sim n_e^2$). As the final result of our work will be a model of the air ICPs at subatmospheric pressures (0.01–0.1 atm) used for atmospheric (re)entry simulations,[2,3] no attention has been paid to an improved modeling of radiation. Radiative effects are expected to be negligibly small at such pressures.[18]

Discretization Procedure
Finite Volume Method
Equations (1–15) are discretized with a conservative cell-centered finite volume method[12] on two different structured meshes. The flowfield is discretized on an inner mesh of n_i cells in the axial direction and n_j cells in the radial direction. The flow variables in cell (i, j) are stored in an array $U_{ij} = (\rho, \rho\boldsymbol{u}, T)_{ij}$. The total set of discrete flow variables is contained in a vector $\boldsymbol{U} = \{U_{ij}; i = 1, \ldots, n_i; j = 1, \ldots, n_j\}$.

The electric field is discretized on a far-field mesh, which coincides with the inner mesh inside the torch but extends into the space surrounding it. Similarly, electric-field variables are stored cellwise in arrays E_{ij}. The total discrete electric field is contained in a vector $\boldsymbol{E}$. Finally, a vector $\boldsymbol{Q}$ containing both the flowfield and the electric-field values is introduced: $\boldsymbol{Q} = (U, E)$.

A straightforward central discretization ensures numerical stability for the Helmholtz-type induction equation and for the viscous fluxes F^d and G^d. A second-order flowfield method is obtained with a total variation diminishing (TVD) reconstruction in the discretization of the convective fluxes F^c and G^c (Ref. 20). Slope limiting needs to be applied in the reconstruction of only the energy fluxes; for the continuity and the momentum fluxes, the unlimited second-order scheme is found to be stable.

Pressure-Stabilized Flowfield Solver
High-pressure ICPs are characterized by low Mach numbers (<0.3) and may therefore be considered incompressible, in the sense that density hardly varies because of pressure variations in the flowfield ($=$ compression). However, most of the traditional approximations of incompressible flow (e.g., $\nabla\cdot\boldsymbol{u} = 0$) do not apply, as density changes dramatically because of the strong temperature variations in the plasma. The vast majority of ICP models we have encountered so far rely on classical SIMPLE-type incompressible flow solvers, in which velocity vectors are represented on a dual, staggered mesh.[11] A more straightforward pressure-stabilized solver on a collocated mesh[12,21] is proposed as an alternative here.

Pressure wiggles are eliminated in a conservative manner when a small dissipative pressure term is added to the convective fluxes F^c and G^c. Consider a cell edge normal to the z direction. Reconstructed

flowfield variables to the left and the right of the edge are written as U_L and U_R, respectively; average reconstructed values on the edge are written as $U_E = (U_L + U_R)/2$. The pressure-stabilized mass flux $\tilde{f}_m$ in the z direction is given by

$$\tilde{f}_m = (\rho u)_E - (\Lambda/\beta)(p_R - p_L) \qquad (16)$$

where β stands for an estimated maximal velocity in the flowfield. The factor Λ is needed to scale the pressure dissipation properly in regions of low cell Reynolds numbers:

$$\Lambda_V = \frac{Re_{\Delta z}}{1 + Re_{\Delta z}}, \qquad Re_{\Delta z} = \frac{\rho \beta \Delta z}{\mu} \qquad (17)$$

Thus, the following stabilized convective flux vector $\tilde{F}^c$ is found:

$$\tilde{F}^c = \begin{bmatrix} \tilde{f}_m \\ \tilde{f}_m u_E - 0.5|\tilde{f}_m|(u_R - u_L) + p_E \\ \tilde{f}_m v_E - 0.5|\tilde{f}_m|(v_R - v_L) \\ \tilde{f}_m w_E - 0.5|\tilde{f}_m|(w_R - w_L) \\ \tilde{f}_m h_E - 0.5|\tilde{f}_m|(h_R - h_L) \end{bmatrix} \qquad (18)$$

Upwind stabilization has been added to the discrete momentum and energy fluxes. Note that the modified mass flux $\tilde{f}_m$ appears in all fluxes. The method can be easily extended to a modern viscous preconditioning method, valid within a wide range of Mach numbers.[22, 23]

Electric-Field Formulation

To our best knowledge, McKelliget[9] first introduced the accurate two-dimensional electric-field formulation used in the vast majority of current high-pressure ICP models. The complete induction equation (1) is solved in the interior of the torch. Every cell in the computational domain is considered as an (infinitely thin) current-carrying loop. The electric-field amplitude at each boundary cell is obtained by adding up the contributions of the outer coil rings and all cells in the computational domain. Although mathematically elegant, this integral boundary procedure is computationally expensive, as it couples every boundary cell to all interior cells. It thereby leads to a nonsparse linear system, which cannot be solved efficiently with state-of-the-art iterative techniques.[24]

The electric-field formulation used here differs from the integral boundary approach in two points. First, when the electric field is solved on a far-field mesh, the expensive integral boundary condition can be replaced with the simple far-field boundary conditions (11), such that the electric-field problem takes a sparse form. Second, singularities near the coil rings are avoided by solving for the plasma-induced electric field rather than the total electric field. Surprisingly few researchers have applied the far-field approach to high-pressure ICP modeling.[16] On the other hand, far-field formulations are widely used in low-pressure ICP models.[10, 25]

The electric-field amplitude E is split in a singular part induced by the outer inductor rings E_V and a nonsingular plasma-induced part E_P:

$$E = E_V + E_P$$

An analytical form for the electric field induced by a single, infinitely thin current-carrying loop can be derived from the Biot–Savart law.[26] The vacuum-field amplitude E_V is then calculated by adding up the contributions of the discrete coil rings constituting the inductor. Induction equation (1) is rewritten under the following regular form:

$$\frac{\partial^2 E_P}{\partial z^2} + \frac{1}{r}\frac{\partial}{\partial r}\left(r\frac{\partial E_P}{\partial r}\right) - \frac{1}{r^2}E_P - i2\pi\mu_0\sigma f(E_P + E_V) = 0$$

$$(19)$$

As the electrical conductivity σ is zero in the entire space outside of the plasma torch, the singularity in E_V does not affect Eq. (19).

Iterative Strategy

Picard Method

A highly robust iterative technique similar to the approaches taken in traditional models is recommended during the initial iterations of the model. The electric field and the flowfield are treated in a decoupled manner. The overall electric-field intensity is adjusted at each iteration such that the power dissipated into the plasma stays constant. The flowfield is updated with a robust Picard iterative method, which remains stable at each iteration. Underrelaxation is applied to enhance stability and convergence.

Electric-Field Solution

For a given flowfield, the electric field is updated by solving Eq. (19) on the far-field domain. The electric-field residual at iteration n is written as R_E^n; a new electric-field value E^{n+1} is obtained by the solution of a sparse linear system on the far-field mesh:

$$J_E^n(E^{n+1} - E^n) = -R_E^n \qquad (20)$$

where J_E^n is referred to as the electric-field Jacobian.

When an ICP model is run for a fixed value of I_C, the power dissipated in the plasma is often found to decrease with each iteration, until eventually a room-temperature solution is obtained. Boulos[7] solved this problem by instead running his model for a fixed power P_0 dissipated into the plasma (see also Ref. 27). The linearity of Eq. (1) implies that E is directly proportional to the current in the outer inductor I_C. Hence the joule heating source term of Eq. (10) depends in a quadratic manner on I_C. One therefore first updates E with Eq. (20) and calculates the total power dissipated into the plasma P_t. Next, the electric field and the coil current are multiplied by a factor γ, where

$$\gamma^2 = P_t/P_0$$

Only thereafter, the Lorentz forces [Eqs. (9)] and joule heating rate [Eq. (10)] are computed in each cell of the numerical domain.

Flowfield Solution

During the initial iterations, severe problems of numerical instability arise in the large temperature gradient regions near the torch inlet. A positive flowfield solution procedure is then very useful. The flowfield values in a cell (i, j) are connected to neighboring cell values by the discretized convective and diffusive terms:

$$U_{ij} = \Sigma_l c_l U_l \qquad (21)$$

where l runs over all neighboring cells. One easily shows that for a first-order upwind discretization of the convective terms, a positive scheme is obtained,[11] such that $0 \leq c_l \leq 1$. The flowfield values in each cell are a convex average of the values in the neighboring cells.

For a given value for the electric field E, the flowfield problem may now be expressed in a matrix form, inspired by the earlier positive stencil of Eq. (21):

$$J_P(U^{n+1} - U^n) = -R_U^n \qquad (22)$$

The right-hand vector R_U^n stands for the first-order flowfield residual at time step n and depends on the electric field. Suppose that an intermediate solution U^n has been obtained. One may obtain new solution U^{n+1} by first evaluating J_P and R_U^n with the solution at step n, and then solving system (22) for $\Delta U = U^{n+1} - U^n$. The positivity of the first-order discretization guarantees the numerical stability of this procedure. When instead the second-order discretization for R_U^n is used in combination with the first-order expression for J_P, it is found that the TVD properties of the higher-order scheme still guarantee numerical stability.

Sparse Linear System Solution

Sparse linear systems (20) and (22) are solved with the generalized minimal residual (GMRES) iterative scheme, which is well suited for the systems with mixed types of eigenvalues found here.[28]

Damping, Underrelaxation

The Picard method usually does not converge unless some damping is brought into the flowfield solution step. This is done at the linear level by damping the flowfield entries in the Picard matrix. The block diagonal $D\{J_P^n\}$ is enlarged as follows:

$$D\{J_P^n\} \rightarrow D\{J_P^n\}(1 + 1/\text{CFL})$$

where the CFL parameter is not unlike the well-known Courant number used in time-stepping methods.[20] CFL numbers of ~ 100 are found to work well on fine meshes. Furthermore, the nonlinear convergence rate was found to improve when the flowfield update ΔU was multiplied by a global underrelaxation factor of 0.5.

Newton Method

Although very robust, the Picard method often converges poorly. Once an intermediate solution has been obtained with this method, it is therefore proposed to continue with Newton's iterative method. It can be shown that, provided a sufficiently good initial solution is used, Newton's method converges to the final solution in a rapid, quadratic manner.

Given an intermediate solution for the flowfield and the electric field Q^n, a better solution is found by solving the following linear system:

$$J_Q^n(Q^{n+1} - Q^n) = -R_Q^n \tag{23}$$

where $R_Q^n = (R_U^n, R_E^n)$ stands for the combined flowfield and electric-field residual at step n. The Jacobian J_Q^n takes the following global block structure:

$$J_Q^n = \begin{bmatrix} J_U^n & J_{U,E}^n \\ J_{E,U}^n & J_E^n \end{bmatrix} \tag{24}$$

where the diagonal entries are given by the decoupled flowfield and electric-field Jacobians:

$$J_U^n = \frac{\partial R_U^n}{\partial U}, \qquad J_E^n = \frac{\partial R_E^n}{\partial E}$$

and the off-diagonal entries represent the following cross derivatives:

$$J_{U,E}^n = \frac{\partial R_U^n}{\partial E}, \qquad J_{E,U}^n = \frac{\partial R_E^n}{\partial U}$$

J_Q^n can be obtained numerically by performing finite differences. From a programmer's standpoint, however, the evaluation of the cross-derivative terms is far from obvious. Moreover, the evaluation of the flowfield Jacobian J_U^n is expensive and memory consuming when a second-order accurate discretization is used. Whereas for a first-order discretization only the nearest neighbors of each cell in the domain need to be considered when the Jacobian is computed, for a second-order discretization the stencil is enlarged to the next neighbors.

Approximate Newton Method

The second-order flowfield Jacobian may be approximated by the first-order Jacobian $\tilde{J}_U^n$. In addition, one could neglect the cross-derivative entries, such that the flowfield and the electric field are updated in a decoupled manner, as was done for the Picard method. The following approximate Newton method is thus obtained:

$$\tilde{J}_Q^n(Q^{n+1} - Q^n) = -R_Q^n \tag{25}$$

where no approximations have been used in the residual expression R_Q^n. The approximate Jacobian $\tilde{J}_Q^n$ is given by

$$\tilde{J}_Q^n = \begin{bmatrix} \tilde{J}_U^n & 0 \\ 0 & J_E^n \end{bmatrix} \tag{26}$$

Although the efficiency of a full Newton method is lost as a consequence of these simplifications, the approximate Newton method already performs substantially better than the Picard method. Damping and underrelaxation procedures similar to those outlined for the Picard method can be applied to enhance the convergence and robustness of the approximate Newton method.

Full Newton Method

A fully coupled Newton method can be implemented in a straightforward manner, by exploiting the fact that the GMRES algorithm uses the full Jacobian expression J_Q^n only in matrix–vector products. These may also be computed through finite differences of the complete, second-order accurate residual:

$$J_Q^n V = (1/\epsilon)(R_Q\{Q^n + \epsilon V\} - R_Q\{Q^n\}) \tag{27}$$

where V stands for any vector appearing in a matrix–vector multiplication in the GMRES solver and ϵ is a small number. Thus, when the linear algebra method involved is suitably modified, the calculation of a full second-order accurate Jacobian [Eq. (24)] involving cross derivatives is avoided. Instead, at each iteration of the linear solve, one residual evaluation [Eq. (27)] needs to be performed.

The modified GMRES algorithm still requires an approximation of the Jacobian matrix, which is used to precondition the linear system; a good preconditioning matrix is essential for the efficiency of Krylov subspace methods.[28] The approximate Newton Jacobian $\tilde{J}_Q^n$ is found to be an effective preconditioner. Note that the reevaluation of computationally expensive thermodynamic and transport models in each GMRES step [Eq. (27)] may be avoided if clever use is made of the derivatives of these models, which have already been obtained while the approximate Jacobian was being computed.

Source Term Linearization

It is known that strongly positive source terms, such as the joule heating term [Eq. (10)], should be treated with care.[11] With an explicit treatment of the joule heating term, the approximate Newton method is found to work very well on a wide range of calculations. This comes down to neglecting the temperature dependence of the electrical conductivity σ when computing the approximate Newton Jacobian [Eq. (26)].

At the nonlinear level, the fully coupled Newton method converges significantly faster than the approximate Newton method only if all terms, including the joule heating source term, are treated implicitly. It should be noted that the gain in convergence at the nonlinear level may then be offset by a slowdown at the linear level, as the linear system (23) to be solved by the GMRES algorithm is poorly diagonally dominant. Powerful preconditioning techniques are needed to overcome this problem (see the next section).

Evaluation of the Model Performance

The model has already been validated on an argon ICP test case[29] set up in collaboration with other researchers developing a similar code.[30] Here, the numerical qualities of the model are evaluated by calculations for a 3-species argon and an 11-species air ICP torch at an operating pressure of 1 atm.

Torch Geometry and Operating Conditions

The torch geometry and operating conditions used for the simulations are shown on Fig. 2; they correspond to the von Kármán Institute minitorch of Fig. 1. The inner and the far-field meshes used for the calculations (Fig. 3) were generated with a simple algebraic mesh generator. The inner mesh contains 86×32 cells; the far-field
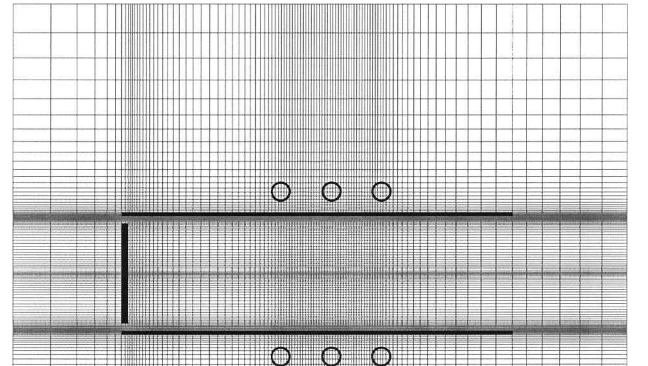

Fig. 3   Mesh used for the numerical simulations (part above axis): inner mesh, 86×32 cells; and far-field mesh, 100×58 cells.

mesh contains 100×58 cells. All presented results are of second-order accuracy. Calculations on finer meshes[29] differ by $\sim 1\%$ from the results shown here.

The electric current in the inductor is known to flow mainly in the part of the coil rings located near the plasma.[31] The infinitely thin current rings representing the inductor are therefore taken to coincide with the inner radius ($r = 19$ mm) rather than with the center radius of the actual coil rings. For the argon calculations, the optically thin radiative losses calculated by Wilbers et al.[18] were included. For the air calculations, no radiative losses needed to be taken into account as temperatures remained relatively low.[19]

Convergence Analysis

Computations were performed on an up-to-date workstation (235 Mflops). The GMRES solver and various preconditioning methods were provided by the AZTEC linear algebra package, which is available free for academic use.[32] For all iterative methods, the GMRES solver was used with a Krylov subspace dimension of 50 and a linear convergence threshold of 10^{-3}. For the Picard and the approximate Newton methods, a BILU(0) preconditioner was used; ~ 20 Mbytes of storage was required. For the full Newton method, a very powerful BILU(3) preconditioner was needed to overcome linear convergence problems caused by the joule heating source term. Although the true memory used for the method was large but still reasonable (62 Mbytes), the current version of AZTEC appeared to allocate a considerable amount of largely unused memory (215 Mbytes) by default when BILU($k > 0$) preconditioners were used. It is hoped that more economic preconditioners will become available in the near future.

Figure 4 shows the convergence histories obtained for the argon and air cases. All calculations were run at a fixed operating power. In both cases, five initial iterations were performed with Picard's method for a CFL number of 100 and a global underrelaxation factor

Argon calculations

Air calculations

Fig. 4   Convergence histories of the calculations.

of 0.5. Usually a good intermediate solution was obtained after just a few Picard iterations when the following set of initial conditions was used[27]:

$$E^0 = E_V, \qquad U^0 = \{p_A, 0, 0, 0, T_A + (10{,}000 - T_A)[(R-r)/R]\}$$
$$(28)$$

where R stands for the inner radius of the quartz tube.

When calculations were continued with Picard's method for the same CFL number and underrelaxation factor, convergence was no longer satisfactory. For the argon case, it is seen that the method converged in an irregular manner. Approximately 560 iterations were needed to converge 10 orders of magnitude; this corresponds to 90 min of CPU time. For the air case, the Picard method produced an oscillating solution, without converging any further. Although the Picard method was shown to be stable, one cannot prove that it should converge for general nonlinear problems. We often needed to play around with underrelaxation parameters to make the Picard method converge on the highly nonlinear ICP problems considered here. It is thought that ICP models solving various sets of equations in a sequential manner may suffer from similar convergence problems.

As an alternative, calculations were continued with the approximate Newton method, for an increased CFL number of 1000 and, again, a global underrelaxation factor of 0.5. Excellent convergence was found for both the argon and the air case. Approximately 120 iterations were needed to converge 10 orders of magnitude, corresponding to 33 min of CPU time for the argon case and 92 min of CPU time for the air case. For the argon case, a speed-up factor of almost 3 is found. For the air case, it is seen that the approximate Newton method still converges well where the Picard method fails.

When the CFL number was increased beyond 1000, the convergence rate of the approximate Newton method did not increase any further. Therefore the full Newton method was switched on once ~ 2 orders of magnitude convergence had been obtained. Rapid Newton convergence was found for both the argon and the air case. Obviously, one full Newton iteration costs more CPU time than an approximate Newton iteration. However, this was more than compensated for by the fact that only 8 full Newton iterations were needed to converge down to more than 11 orders of magnitude.
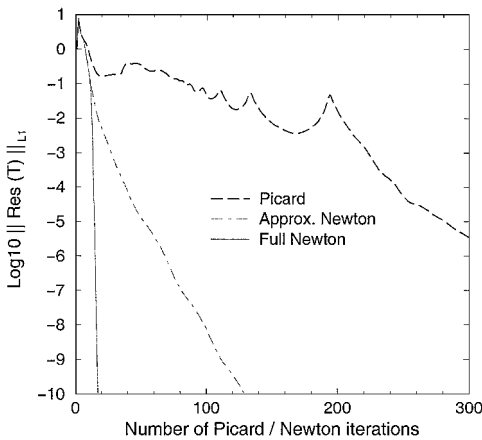
For the argon case, 18 combined Picard and Newton iterations were needed to converge, corresponding to ~ 9 min of overall CPU time. This is almost 4 times faster than when the approximate Newton method is used and 10 times faster than when the Picard method is used. For the air case, 23 combined Picard and Newton iterations were needed, corresponding to only 22 min of overall CPU time. Compared with the approximate Newton method, a speed-up factor of more than 4 is found.
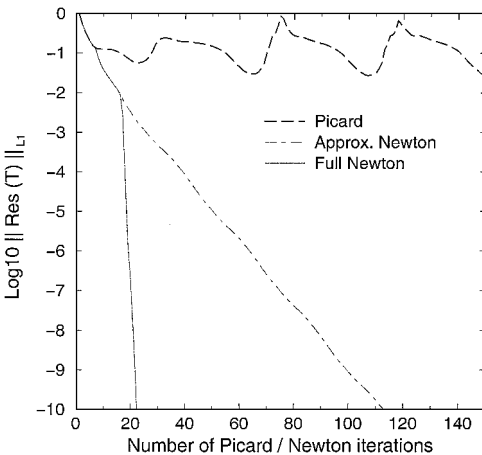
Flow, Temperature, and Electric-Field Results

Figure 5 shows the computed temperature contours and streamlines for the argon case. Peak temperatures of $\sim 10{,}000$ K are found at an off-axis position. The plasma is heated in a narrow skin layer close to the torch wall. Radiative losses cool the plasma around the torch axis where no joule heating takes place, causing maximum temperatures to shift farther away from the axis. The clockwise recirculations seen in the flowfield are caused by both viscous entrainment and by the radially directed Lorentz forces in in the inductor region.[7] Because of the swirling flow injection, centrifugal forces cause the clockwise recirculations to lift away from the axis and give rise to a secondary, counterclockwise recirculation.

Figure 6 shows the computed temperature contours and streamlines for the air case. In molecular gases, a considerable amount of energy is needed to dissociate molecules before ionization occurs. This explains why much lower peak temperatures of ~ 8000 K are found for the air calculations. Because of the absence of radiative losses, peak temperatures appear close to the axis. Calculations of other researchers for comparable five-species nitrogen plasmas yield similar temperature fields.[33]

Figure 7 shows the computed total electric-field amplitude $E_P + E_V$ for the argon case. A pattern similar to the one obtained by Yang et al.[34] is found. Axial variations are seen to be relatively

Temperature contours (in degrees Kelvin)

Streamlines

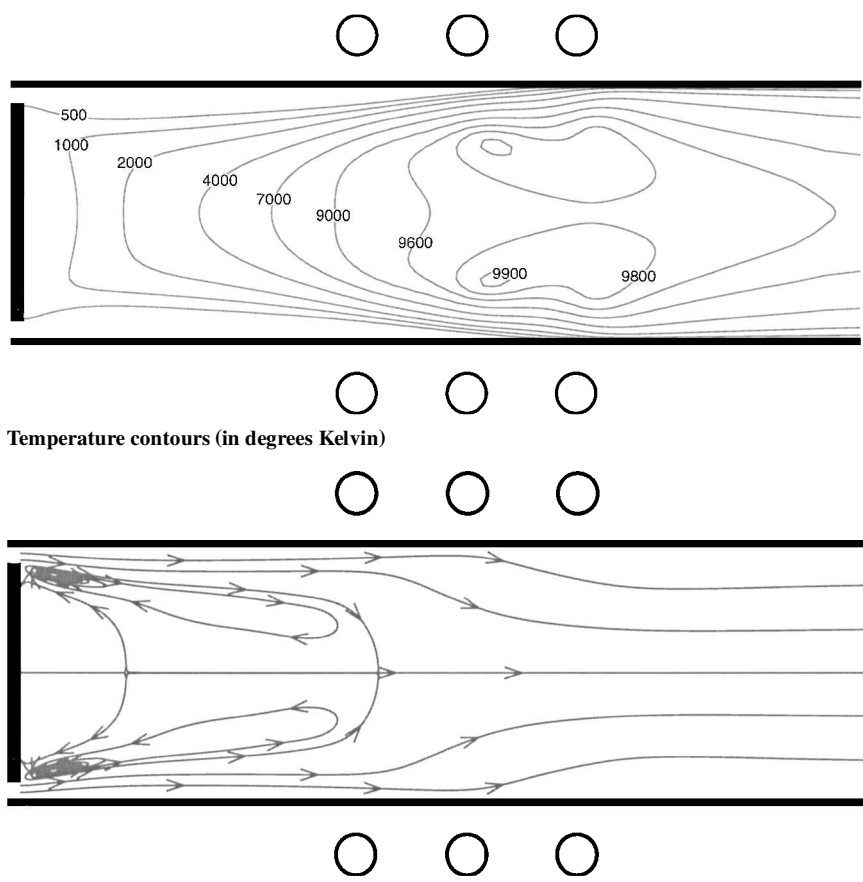**Fig. 5 Argon ICP torch.**

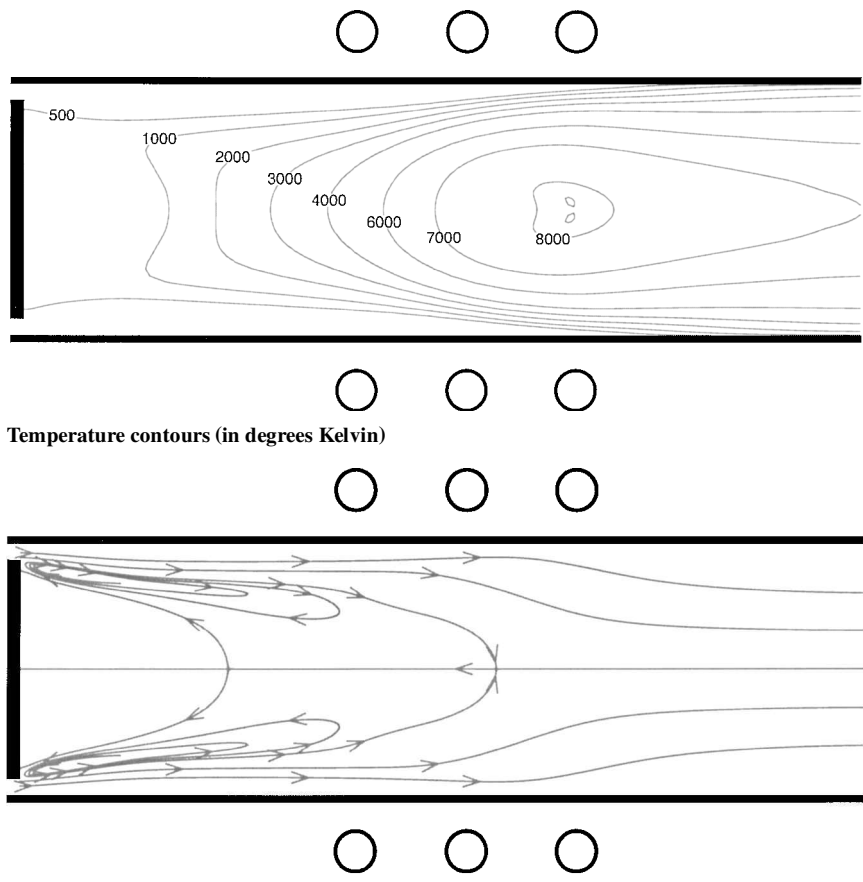Temperature contours (in degrees Kelvin)

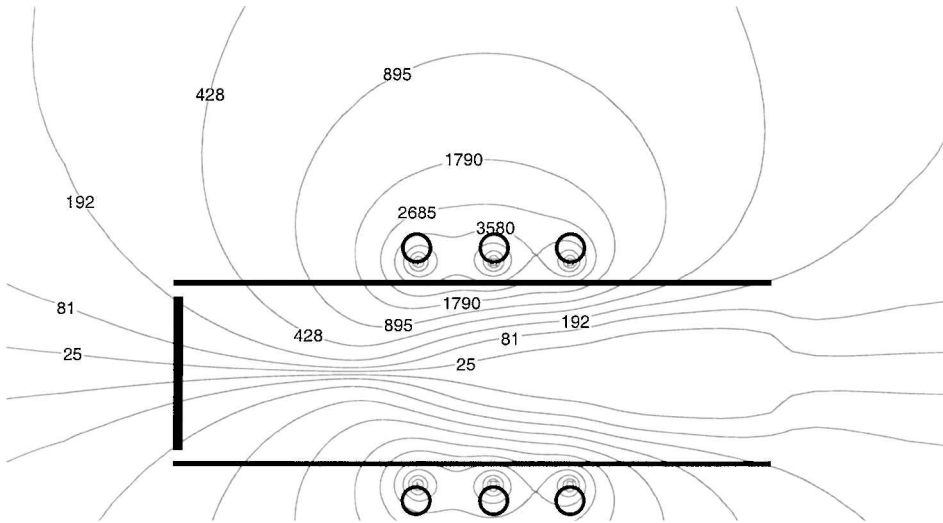Streamlines

Fig. 6 Air ICP torch.

Fig. 7   Argon ICP torch: contours of total electric-field amplitude (in volts per meter).
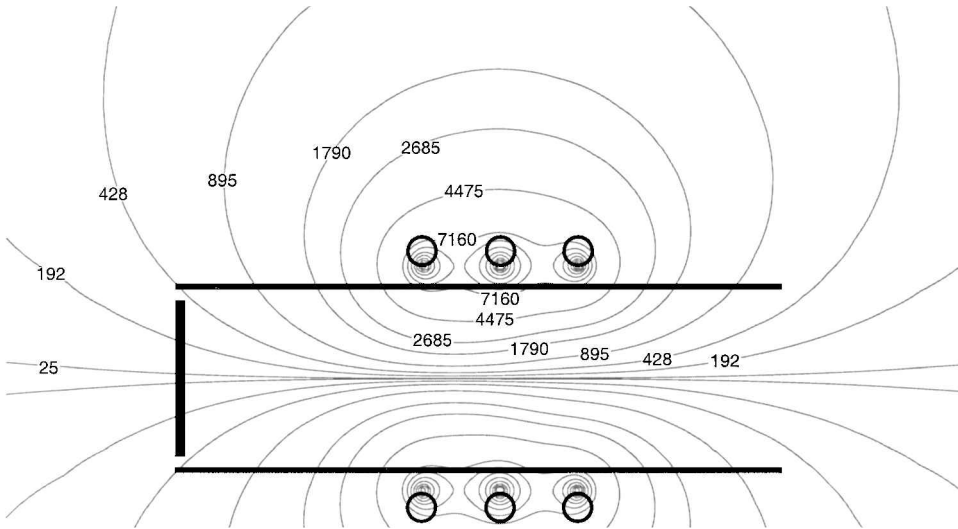

Fig. 8   Air ICP torch: contours of total electric-field amplitude (in volts per meter).

important; this supports the use of the accurate two-dimensional electromagnetic-field formulation (19) rather than a simple one-dimensional formulation.[30] The sudden bend in the isolines near the torch outlet is caused by the neglect of ionization beyond the outlet. Figure 8 shows the computed electric-field amplitude for the air case. Because of the higher operating power used, the electric field is considerably stronger than that for the argon case. Because of the low temperatures, electrical conductivities in the plasma are low and the overall electric field E is close to its vacuum value E_V.

Conclusion

The presented ICP model aims at improving the accuracy and efficiency of the existing high-pressure ICP models. New discretization techniques were suggested for both the flowfield and the electromagnetic-field equations. Powerful iterative methods were proposed to solve the nonlinear system of discretized equations in an optimal manner.

The governing equations are discretized with a cell-centered finite volume method. A second-order TVD discretization is used to stabilize convective terms in the flowfield equations. The low Mach number flow field is computed with a modern pressure-stabilized solver on a collocated mesh, rather than with a traditional staggered-mesh solver. A small dissipative pressure term is added to the otherwise centrally discretized mass fluxes in the continuity equation. Convective momentum and energy fluxes need to be discretized in a manner consistent with the modified mass fluxes.

The two-dimensional electric field is solved for on a far-field mesh, which coincides with the flowfield mesh inside the torch, but extends into the surrounding space. Thus, the electromagnetic-field problem takes the form of a sparse linear system, which can be solved efficiently by means of state-of-the-art iterative methods.

Various iterative solution strategies have been implemented and tested. During the initial iterations, in which numerical stability is the main concern, the electric field and the flowfield are updated in a decoupled manner by a robust Picard method. Linear systems are solved with a preconditioned GMRES algorithm. Once an acceptable intermediate solution has been obtained with the Picard strategy, calculations are continued with an approximate Newton method in which electromagnetic/flowfield coupling terms in the Jacobian matrix are still neglected. Finally, after a few approximate Newton iterations, the calculation can be continued with a fully coupled Newton method, in which the matrix–vector products in the GMRES algorithm are computed with a Jacobian-free finite difference approximation.

The performance of the new model was evaluated through calculations of an LTE argon and air inductive plasma. Provided a good initial solution was chosen, five iterations with the Picard method were sufficient to obtain a rough intermediate solution. Although of great help in the initial iterations because of its robustness, the Picard method did not converge well in the subsequent iterations. When the calculation was continued with the approximate Newton method, however, excellent convergence was found; ~120 iterations

were needed to converge 10 orders of magnitude. Once a reasonably good intermediate solution had been obtained, the full Newton method could be used to converge in a rapid, quadratic manner; only eight full Newton iterations were needed to reach more than 11 orders of magnitude convergence. The fully coupled method converged four times quicker than the approximate method and 10 times quicker than the Picard method.

The proposed full Newton method was found to converge significantly faster at the nonlinear level only if the joule heating source term was taken into account implicitly. A highly memory-consuming BILU(3) preconditioner was needed to overcome associated convergence problems at the linear level. It is hoped that more economic preconditioning techniques will become available in the near future. We always managed to converge in reasonable CPU times with the approximate Newton method. Considering both the speed of convergence and the use of memory, the approximate Newton method may therefore be considered optimal.

Acknowledgments

References

[1]Boulos, M. I., "Radio Frequency Plasma Developments, Scale-Up and Industrial Applications," *High Temperature Chemical Processes*, Vol. 1, No. 4, 1992, pp. 401–411.

[2]Bottin, B., Carbonaro, M., Vander Haegen, V., and Paris, S., "Predicted and Measured Capability of the VKI 1.2 MW Plasmatron Regarding Re-Entry Simulation," ESA SP-426, ESTEC, Noordwijk, The Netherlands, 1999.

[3]Kolesnikov, A. F., "Aerothermodynamic Simulation in Sub- and Supersonic High-Enthalpy Jets: Experiment and Theory," ESA SP-367, ESTEC, Noordwijk, The Netherlands, 1994.

[4]Bukowski, J. D., Graves, D. B., and Vitello, P., "Two-Dimensional Model of an Inductively Coupled Plasma with Comparison to Experimental Spatial Profiles," *Journal of Applied Physics*, Vol. 80, No. 5, 1996, pp. 2614–2623.

[5]Miller, R. C., and Ayen, R. J., "Temperature Profiles and Energy Balances for an Inductively Coupled Plasma Torch," *Journal of Applied Physics*, Vol. 40, No. 13, 1996, pp. 5260–5273.

[6]Boulos, M. I., "The Inductively Coupled Radio Frequency Plasma," *Pure and Applied Chemistry*, Vol. 57, No. 9, 1985, pp. 1321–1352.

[7]Boulos, M. I., "Flow and Temperature Fields in the Fire-Ball of an Inductively Coupled Plasma," *IEEE Transactions on Plasma Science*, Vol. PS-4, No. 1, 1976, pp. 28–39.

[8]Mostaghimi, J., Proulx, P., and Boulos, M. I., "An analysis of the Computer Modeling of the Flow and Temperature Fields in an Inductively Coupled Plasma," *Journal of Numerical Heat Transfer*, Vol. 8, No. 1, 1985, pp. 187–201.

[9]McKelliget, J. W., "A Mathematical Model of an Inductive Plasma Torch," College of Engineering, TR 86-112.1, Univ. of Lowell, Lowell, MA, Sept. 1986.

[10]Jaeger, E. F., Berry, L. A., Tolliver, J. S., and Batchelor, D. B., "Power Deposition in High-Density Inductively Coupled Plasma Tools for Semiconductor Processing," *Physics of Plasmas*, Vol. 2, No. 6, 1995, pp. 2597–2604.

[11]Patankar, S. V., *Numerical Heat Transfer and Fluid Flow*, McGraw–Hill, New York, 1980.

[12]Ferziger, J. H., and Perić, M., *Computational Methods for Fluid Dynamics*, Springer, Berlin, 1996.

[13]Mostaghimi, J., Proulx, P., and Boulos, M. I., "A Two-Temperature Model of the Inductively Coupled RF Plasma," *Journal of Applied Physics*, Vol. 61, No. 5, 1987, pp. 1753–1760.

[14]Mostaghimi, J., and Boulos, M. I., "Effect of Frequency on Local Thermodynamic Equilibrium Conditions in an Inductively Coupled Argon Plasma at Atmospheric Pressure," *Journal of Applied Physics*, Vol. 68, No. 6, 1990, pp. 2643–2648.

[15]Chen, X., and Pfender, E., "Modelling of RF Plasma Torch with a Metallic Tube Inserted for Reactant Injection," *Plasma Chemistry and Plasma Processing*, Vol. 11, No. 1, 1991, pp. 103–128.

[16]Mekideche, M. R., "Contribution à la Modélisation Numérique de Torches à Plasma d'Induction," Ph.D. Dissertation, École Doctorale Sciences pour L'Ingénieur de Nantes, St. Nazaire, France, Oct. 1993.

[17]Bottin, B., Vanden Abeele, D., Carbonaro, M., Degrez, G., and Sarma, G. S. R., "Thermodynamic and Transport Properties for Inductive Plasma Modeling," *Journal of Thermophysics and Heat Transfer*, Vol. 13, No. 3, 1993, pp. 343–350.

[18]Wilbers, A. T. M., Beulens, J. J., and Schram, D. C., "Radiative Energy Loss in a Two-Temperature Argon Plasma," *Journal of Quantitative Spectroscopy and Radiative Transfer*, Vol. 46, No. 5, 1991, pp. 387–392.

[19]Dresvin, S. V., Donskoi, A. V., Goldfarb, V. M., and Klubnikin, V. S., *Physics and Technology of Low-Temperature Plasmas*, edited by H. V. Eckert, Iowa State Univ. Press, Ames, IA, 1977, p. 355.

[20]LeVeque, R. J., *Numerical Methods for Conservation Laws*, Birkhauser, Basel, Switzerland, 1990, p. 183.

[21]Benoy, D. A., "Modeling of Thermal Argon Plasmas," Ph.D. Dissertation, Technical Univ. of Eindhoven, Eindhoven, The Netherlands, April 1993.

[22]Choi, Y.-H., and Merkle, C. L., "The Application of Preconditioning in Viscous Flows," *Journal of Computational Physics*, Vol. 105, No. 2, 1993, pp. 207–223.

[23]Weiss, J. M., and Smith, W. A., "Preconditioning Applied to Variable and Constant Density Flows," *AIAA Journal*, Vol. 33, No. 11, 1995, pp. 2050–2057.

[24]Vanden Abeele, D., and Degrez, G., "An Efficient Computational Model for Inductive Plasma Flows," AIAA Paper 98-2825, June 1998.

[25]Lymberopoulos, D. P., and Economou, D. J., "Two-Dimensional Simulation of Polysilicon Etching with Chlorine in a High Density Plasma Reactor," *IEEE Transactions on Plasma Science*, Vol. 23, No. 4, 1995, pp. 573–580.

[26]Silvester, P., *Modern Electromagnetic Fields*, Prentice–Hall, Englewood Cliffs, NJ, 1968, p. 153.

[27]Yu, B. W., and Girshick, S. L., "Modeling Inductively Coupled Plasmas: The Coil Current Boundary Condition," *Journal of Applied Physics*, Vol. 69, No. 2, 1991, pp. 656–661.

[28]Saad, Y., *Preconditioned Krylov Subspace Methods: An Overview; Computational Fluid Dynamics Review 1995*, Wiley, New York, 1995.

[29]Vanden Abeele, D., Vasil'evskii, S. A., Kolesnikov, A. F., Degrez, G., and Bottin, B., "Code-to-Code Validation of Inductive Plasma Computations," von Kármán Inst. for Fluid Dynamics, VKI TN 197, St. Genesius-Rode, Belgium, July 1999.

[30]Vasil'evskii, S. A., Kolesnikov, A. F., and Yakushin, M. I., "Mathematical Models for Plasma and Gas Flows in Induction Plasmatrons," *Molecular Physics and Hypersonic Flows*, edited by M. Capitelli, Kluwer, Dordrecht, The Netherlands, 1996, pp. 495–504.

[31]Fouladgar, J., and Chentouf, A., "The Calculation of the Impedance of an Induction Plasma Installation by a Hybrid Finite-Element Boundary-Element Method," *IEEE Transactions on Magnetics*, Vol. 29, No. 6, 1993, pp. 2479–2481.

[32]Hutchinson, S., Prevost, L., Shadid, J., Tong, C., and Tuminaro, R., "Official Aztec User's Guide: Version 2.0," Sandia National Labs., Sandia TR SAND99-8801J, Albuquerque, NM, 1999.

[33]Mostaghimi, J., Proulx, P., and Boulos, M. I., "Parametric Study of the Flow and Temperature Fields in an Inductively Coupled RF Plasma Torch," *Plasma Chemistry and Plasma Processing*, Vol. 4, No. 3, 1984, pp. 199–217.

[34]Yang, P., Barnes, R. M., Mostaghimi, J., and Boulos, M. I., "Application of a Two-Dimensional Model in the Simulation of an Analytical Inductively Coupled Plasma Discharge," *Spectrochimica Acta*, Vol. 44B, No. 7, 1989, pp. 657–666.